The Astrophysical Journal Letters, 946:L7 (7pp), 2023 March 20 https://doi.org/10.3847/2041-8213/acc4b7

The Chocolate Chip Cookie Model: Dust-to-metal Ratio of H II Regions

Jiafeng Lu (卢家风)[1,2], Shiyin Shen (沈世银)[1,3], Fang-Ting Yuan (袁方婷)[1,3], and Qi Zeng (曾琪)[1,2]
[1] Key Laboratory for Research in Galaxies and Cosmology, Shanghai Astronomical Observatory, Chinese Academy of Sciences, 80 Nandan Road, Shanghai 200030, People's Republic of China; ssy@shao.ac.cn
[2] University of Chinese Academy of Sciences, 19A Yuquan Road, Beijing 100049, People's Republic of China
[3] Key Lab for Astrophysics, Shanghai, 200034, People's Republic of China
Received 2023 February 5; revised 2023 March 6; accepted 2023 March 16; published 2023 April 3

Abstract

Using a sample of face-on star-forming galaxies selected from the Sloan Digital Sky Survey, we statistically derive the typical optical depth $\tau_{\rm cl}$ of individual H II regions based on the "Chocolate Chip Cookie" model of Lu et al. (2022). By binning galaxies into stellar mass and gas-phase metallicity bins and interpreting $\tau_{\rm cl}$ as the dust-to-gas ratio (DGR) of H II regions, we further investigate the correlations between DGR and stellar mass and between DGR and gas-phase metallicity, respectively. We find that DGR increases monotonically with the stellar mass of galaxies. At a given stellar mass, DGR shows a linear correlation with the gas-phase metallicity, which implies a constant dust-to-metal ratio (DTM) of galaxies at a given stellar mass. These results adequately indicate that the DTM of galaxies is simply a function of their stellar masses. In terms of gas-phase metallicity, because of the mass–metallicity relation, DTM increases with increasing metallicity with a power-law index 1.45 in the low-metallicity region, while it remains constant at the high-metallicity end.

Unified Astronomy Thesaurus concepts: Disk galaxies (391); Extinction (505); Interstellar dust (836); Interstellar dust extinction (837); H II regions (694); Gas-to-dust ratio (638)

1. Introduction

Dust plays an important role in star formation and galaxy evolution. The properties of dust in galaxies, particularly the dust-to-gas ratio (DGR) and dust-to-metal ratio (DTM), have been intensively studied through statistical scaling relations (Lisenfeld & Ferrara 1998; Hirashita et al. 2002; Draine et al. 2007; Galametz et al. 2011; Zafar & Watson 2013; Rémy-Ruyer et al. 2014; Wiseman et al. 2017; Kahre et al. 2018; De Vis et al. 2019). Dust-evolution models show that the growth of dust grains increases DTM (Mattsson et al. 2012), while dust destruction performs in the opposite way (Draine & Salpeter 1979). Therefore, in observation, the DGR or DTM as a function of metallicity provides an effective constraint on dust-evolution mechanisms. Early studies have suggested a linear relation between DGR and metallicity, or a constant DTM (Issa et al. 1990; Lisenfeld & Ferrara 1998), for a wide range of galaxies, which was explained by the ineffectiveness of grain growth and destruction (Hirashita 1999; Edmunds 2001). A constant DTM is also assumed in many semianalytic models and hydrodynamical simulations (Silva et al. 1998; James et al. 2002; Somerville et al. 2012; Camps et al. 2015; Yajima et al. 2015; Clark et al. 2016; Katz et al. 2019; Ma et al. 2019). In recent studies, a variable-metallicity-dependent DTM has been widely presented by infrared (IR) observations, especially for galaxies with low metallicity (for example, Rémy-Ruyer et al. 2014; De Vis et al. 2017, 2019). However, selection effects or uncertainties could result in different observational trends because of the small sample size of a few hundred galaxies (Mattsson et al. 2014).

The large galaxy samples in optical survey are more suitable for statistical study. However, it is not straightforward to derive the DGR or DTM from the optical observations alone. With spectroscopic observations, the gas-phase metallicity of star-forming galaxies (SFGs) can be easily derived from the emission lines of H II regions (for example, Tremonti et al. 2004). Therefore, if we can have an implicit probe of the average amount of dust (i.e., optical depth) of the H II regions of SFG using optical observations, we could study the dependence of DGR (or DTM) on the other physical properties of galaxies statistically with a large sample. However, the statistical estimation of the average amount of dust (optical depth) of H II regions in extragalactic galaxies is nontrivial. First of all, we cannot get the observational constraint on the optical depth of H II regions through the reddening of the emission lines directly. The emission lines of H II regions are not only extincted by the dust layer of themselves but also extincted by the foreground interstellar medium (ISM) along the line of sight. Moreover, considering the clumpy distribution of H II regions along the line of sight, especially when the disk galaxies are highly inclined, there will be a intercovering effect of H II regions, which will certainly result in a biased estimation of the average dust extinction of H II regions.

Recently, Lu et al. (2022) have provided a framework of the dust configuration of disk galaxies named the "Chocolate Chip Cookie" (hereafter CCC) model, in which the clumpy nebular regions are embedded in a diffuse stellar/ISM disk, like chocolate chips in cookies. In this model, the average optical depth of individual H II regions $\tau_{\rm cl}$ is a model parameter, which can be well constrained because both the foreground ISM dust extinction and the mutual attenuation of H II clumps have been carefully considered. Moreover, as we will show in Section 2, for face-on galaxies, the derivation of the optical depth of individual H II regions could be even simplified. That is to say, using the CCC model, we can obtain the typical optical depth of the H II regions and then estimate the DTM for a given sample of SFGs based on the optical observation data alone.

In this work, we aim to derive the average optical depth of individual H II regions, $\tau_{\rm cl}$, via an approximation of the CCC model with a sample of face-on SFG in the Sloan Digital Digital Sky Survey (SDSS). Then, we explore the dependence of $\tau_{\rm cl}$ on the stellar mass and gas-phase metallicity of galaxies, which gives us more details about the variations of DTM and puts constraints on the possible physical mechanisms of these variations.

The outline of this paper is as follows. In Section 2, we present a face-on SFG sample and show their dust-reddening features. In Section 3, we introduce a method to interpret DTM as a function of $\tau_{\rm cl}$ and gas-phase metallicity. Then, we use the simplified "CCC model" to derive $\tau_{\rm cl}$ for different subsamples of galaxies. We present our main results in Section 4 and discuss the DTM of SFGs in Section 5. Finally, we give a summary in Section 6.

2. Data: Face-on Disk Galaxy Sample

In this study, we use the SFG sample of Lu et al. (2022), which was selected from the spectroscopic main sample galaxies of the SDSS using the Baldwin–Phillips–Terlevich diagram applied with the criteria of Kauffmann et al. (2003a) and requiring the signal-to-noise ratio (S/N) of each emission lines larger than 3. Unlike the Milky Way–like (MW-like) galaxies studied in Lu et al. (2022), we apply the CCC model to galaxies in a much larger stellar mass range ($9 < \log M_* < 11$, where M_* represents the stellar mass in unit of solar mass). Moreover, we further select the face-on SFGs with an axis ratio $b/a > 0.8$ to simplify the CCC model so that the constraints on the optical depth of the H II regions can be more explicitly obtained (see Section 3 for detail). We therefore finally obtain a sample of 25,573 face-on SFGs within the stellar mass range $9 < \log M_* < 11$. In our sample, the gas-phase metallicity (12 +log(O/H)) is obtained from the MPA-JHU database,[4] following Tremonti et al. (2004).

Following the same method as Lu et al. (2022), we first obtain the stellar reddening $E_{\rm s}$ and the emission-line reddening $E_{\rm g}$ for each sample galaxy. In short, the stellar reddening $E_{\rm s}$ is obtained via the stellar population synthesis code STARLIGHT (Cid Fernandes et al. 2005) with the BC03 single stellar population (Bruzual & Charlot 2003). The emission-line reddening $E_{\rm g}$ is obtained via Balmer decrement.

We show the resulting M_*–$E_{\rm s}$ and M_*–$E_{\rm g}$ density distribution in Figure 1. The medians of $E_{\rm g}$ and $E_{\rm s}$ in stellar mass bins of 0.2 dex are connected with black solid lines, while the black dashed lines are the enclosed contours between the 16th percentile and the 84th percentile of $E_{\rm g}$ or $E_{\rm s}$ distribution. Moreover, at a given stellar mass bin, we further divide the sample galaxies into three metallicity bins with an equal number of galaxies and calculate their median $E_{\rm s}$ and $E_{\rm g}$, respectively, which are shown as the colored dots in Figure 1. We also estimate the uncertainties of the median $E_{\rm g}$ and $E_{\rm s}$ in each stellar mass and metallicity bin using the formula $\sqrt{\frac{\pi}{2}}\frac{\sigma}{\sqrt{n}}$, where σ is the standard deviation of $E_{\rm s}$ or $E_{\rm g}$ distribution, and n is the number of galaxy samples in each bin. These uncertainties are also plotted in Figure 1 as the error bar on each colored dot and will be used to estimate the uncertainties $\tau_{\rm cl}$ in Section 3. As shown in Figure 1, $E_{\rm s}$ shows a plateau at 0.1 for low stellar mass ($\log M_* < 9.5$), then increases slightly from 0.1 to 0.15 with stellar mass in the range of $9.5 < \log M_* < 11$, while $E_{\rm g}$ increases monotonically from 0.1 to 0.5 with stellar mass. At a given stellar mass, both $E_{\rm g}$ and $E_{\rm s}$ further increase with the increase of metallicity.

[4] https://wwwmpa.mpa-garching.mpg.de/SDSS/DR7/oh.html

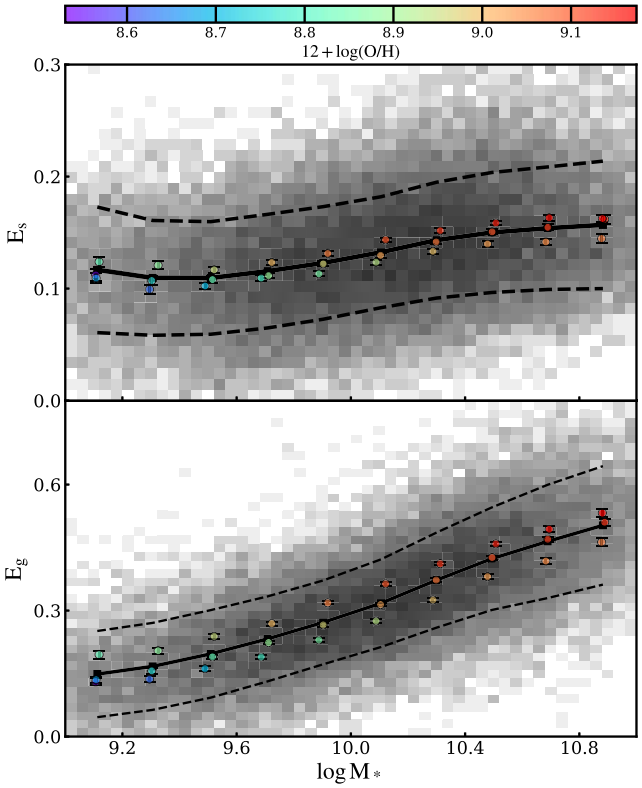

Figure 1. The stellar reddening $E_{\rm s}$ (top panel) and nebular reddening $E_{\rm g}$ (bottom panel) as a function of stellar mass for face-on SFGs. In each panel, the black line represents the median $E_{\rm s}$ (or $E_{\rm g}$), where the two black dashed lines are the 16th and 84th percentiles of $E_{\rm s}$ (or $E_{\rm g}$) respectively. For each stellar mass bin, the colored dots further show the median $E_{\rm s}$ (or $E_{\rm g}$) of three different metallicity bins, which are color-coded according to the color bar plotted on the top of the figure.

It is important to note that our measurement of $E_{\rm g}$ does not directly represent the dust extinction (optical depth) of the H II region itself. However, with these two measurements ($E_{\rm g}$ and $E_{\rm s}$), as we will show in Section 3, our CCC model can easily and robustly estimate $\tau_{\rm cl}$ for face-on SFGs.

3. Method: Deriving Optical Depth of Individual H II Regions

Before deriving the typical optical depth $\tau_{\rm cl}$ of individual H II regions, we first discuss how $\tau_{\rm cl}$ could represent the dust abundance of H II regions. We assume a simple model of a sphere with a dust shell for H II regions. For the inner sphere, the gas is fully ionized, and we assume there is no dust. In the outer shell, the dust is uniformly mixed with the neutral gas. The metallicity is assumed to be the same for the ionized gas of the inner sphere and the neutral gas of the outer shell. With this toy model, We write $\tau_{\rm cl}$ in the form

$$\tau_{\rm cl} = \kappa_V \rho_{\rm dust} l, \quad (1)$$

where $\rho_{\rm dust}$ is the volume density of the dust particles in the outer shell, l is the thickness of the dust shell, and κ_V is the dust absorption coefficient. By linking $\rho_{\rm dust}$ to the DTG and neutral

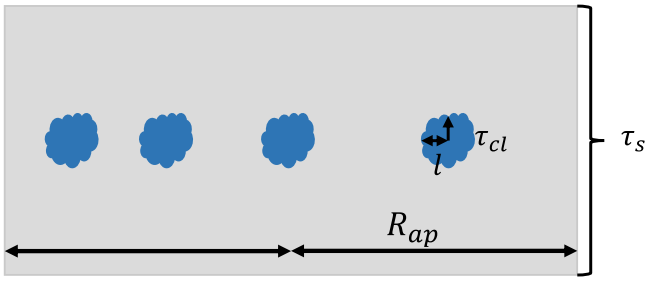

Figure 2. Sketch diagram of simplified CCC model for a face-on disk galaxy inside a fiber aperture (radius $R_{\rm ap}$), where a single layer of individual H II regions (blue clouds; intrinsic optical depth $\tau_{\rm cl}$, and dust-shell thickness l) is sparsely embedded in the middle of a thick ISM disk (gray background; total optical depth $\tau_{\rm s}$ along the line of sight).

gas volume density of shell $\rho_{\rm gas}$, we get

$$\tau_{\rm cl} = \kappa_V \rho_{\rm gas} l \cdot {\rm DTG}. \quad (2)$$

In Equation (2), $\rho_{\rm gas}$ and l parameterize the basic geometric properties of the shell of H II regions, and κ_V characterizes the physical properties of dust particles.

Here, we assume that $\rho_{\rm gas}$, l, and κ_V are all independent of their host galaxies. Considering the the average electron density and size distribution of H II regions are similar for all types of local SFGs (Oey et al. 2003; Liu et al. 2013; Santoro et al. 2022) and the inner ionized sphere and dust shell are both a part of H II complex, the assumption is somewhat reasonable. We therefore get $\tau_{\rm cl} \propto {\rm DTG}$. With this assumption, we will use $\tau_{\rm cl}$ to represent the DTG of galaxies and then study its dependence on other physical properties of galaxies.

The DTG can be further written as the product of DTM (denoted as ζ) and metallicity Z. In this study, we use the gas-phase metallicity estimated by Tremonti et al. (2004), which is defined as the logarithmic abundance ratio of oxygen to hydrogen and denoted as $12 + \log({\rm O/H})$. Therefore, in logarithmic space, the relation between ζ and $\tau_{\rm cl}$ is

$$C + \log\zeta = \log\tau_{\rm cl} - \log({\rm O/H}), \quad (3)$$

where the constant term C represents the unknown and unrelated constant factors assumed in this study (e.g., κ_V, $\rho_{\rm gas}$, and l in Equation (2)).

In Lu et al. (2022), we have presented a two-component dust geometry model for disk galaxies, the CCC model, where the H II regions ("chocolate chips") are embedded in a continuously distributed ISM disk ("cookie"). In the CCC model, the diffuse ISM is assumed to be uniformly mixed with the stellar component, whereas the H II regions are clumpy and distributed in a much thinner disk.

For face-on galaxies, this model can be further simplified to a scenario in which a single layer of H II regions is sparsely embedded in the middle of a thick ISM disk, as illustrated in Figure 2. In Lu et al. (2022), we have obtained that the cross section of H II regions in the central region of MW-like galaxies is 0.84 kpc^{-1} (defined as the average number of H II regions in the central line of sight) and the H II disk has a very low thickness (scale height $\sim$0.1 kpc). For face-on MW-like galaxies, the covering factor of the H II regions inside a fiber aperture is about 0.1 so that the obscuration of the H II regions to the stars is negligible. In this study, we assume all SFGs have a dust geometry configuration similar to MW-like galaxies and make two reasonable assumptions for all face-on SFGs: (1) there is at most one H II region along any single line of sight; and (2) the covering factor of H II regions is very low.

With these two assumptions, the stellar emission is only attenuated by the ISM dust, and the H II nebular emission is attenuated by the ISM dust and the dust shell of the H II region itself. Since the ISM dust is assumed to be uniformly mixed with stellar population in the CCC model, the stellar attenuation and the emission-line attenuation can be simplified as the uniform mixture model and the screen model, respectively, which have also been discussed in Lu et al. (2022). In addition, as the typical size of H II regions is much smaller than the scale height of the stellar disk, the optical depth of the foreground ISM dust of H II regions can be approximated by half of the total optical depth of ISM dust. Finally, the stellar and nebular reddening are then both functions of optical depths:

$$\begin{aligned} E_{\rm s} &= 2.5\log\left(\frac{\tau_{{\rm s},B}}{\tau_{{\rm s},V}}\frac{1-e^{-\tau_{{\rm s},V}}}{1-e^{-\tau_{{\rm s},B}}}\right) \\ E_{\rm g} &= 1.086(\tau_{{\rm g},{\rm H}\beta} - \tau_{{\rm g},{\rm H}\alpha}) \\ \tau_{\rm g} &= \frac{\tau_{\rm s}}{2} + \tau_{\rm cl}, \end{aligned} \quad (4)$$

where $\tau_{\rm s}$ is the total optical depth of ISM dust (see Figure 2), $\tau_{\rm g}$ is the total optical depth of the nebular region along the line of sight, and $\tau_{\rm cl}$ is the optical depth of individual H II regions only.

Based on Equation (4), $\tau_{\rm s}$ and $\tau_{\rm cl}$[5] can be derived from the observed $E_{\rm g}$ and $E_{\rm s}$ by assuming an extinction curve. Following Lu et al. (2022), we assume a power-law attenuation curve with the typical total to selective extinction $R_V = 3.1$ (Li et al. 2017; Fitzpatrick et al. 2019):

$$\frac{A_\lambda}{A_V} = \left(\frac{\lambda}{5500\ {\rm Å}}\right)^{-1.32}. \quad (5)$$

As we have shown in Lu et al. (2022), when given a certain geometry of dust and stars, this extinction curve can reproduce the classical attenuation curve of the Calzetti law (Calzetti et al. 2000).

It should be noted that the CCC model deduces $\tau_{\rm cl}$ of individual H II regions from a statistical perspective. Moreover, instead of deriving $\tau_{\rm cl}$ for each individual galaxy using Equation (4), we take the median $E_{\rm g}$ and $E_{\rm s}$ for a sample of galaxies with similar physical properties and calculate their typical $\tau_{\rm cl}$ values. Meanwhile, the uncertainties of $\tau_{\rm cl}$ are derived by propagating the uncertainties of $E_{\rm g}$ and $E_{\rm s}$. In other words, the motivation of this Letter is to study the $\tau_{\rm cl}$ of SFGs in a statistical sense, rather than focusing on the specific values of $\tau_{\rm cl}$ for any individual galaxy.

4. Results

In Section 2, we divide the face-on SFGs into ten stellar mass bins with bin width of 0.2 dex, and then the galaxies at given stellar mass bin are further divided into subsamples of three gas-phase metallicity bins with equal numbers. In this section, we take these subsamples and explore the variation of $\tau_{\rm cl}$ as function of stellar mass M_* and metallicity

[5] In this paper, if not explicitly specified, the optical depth is defined in the default wavelength V band.

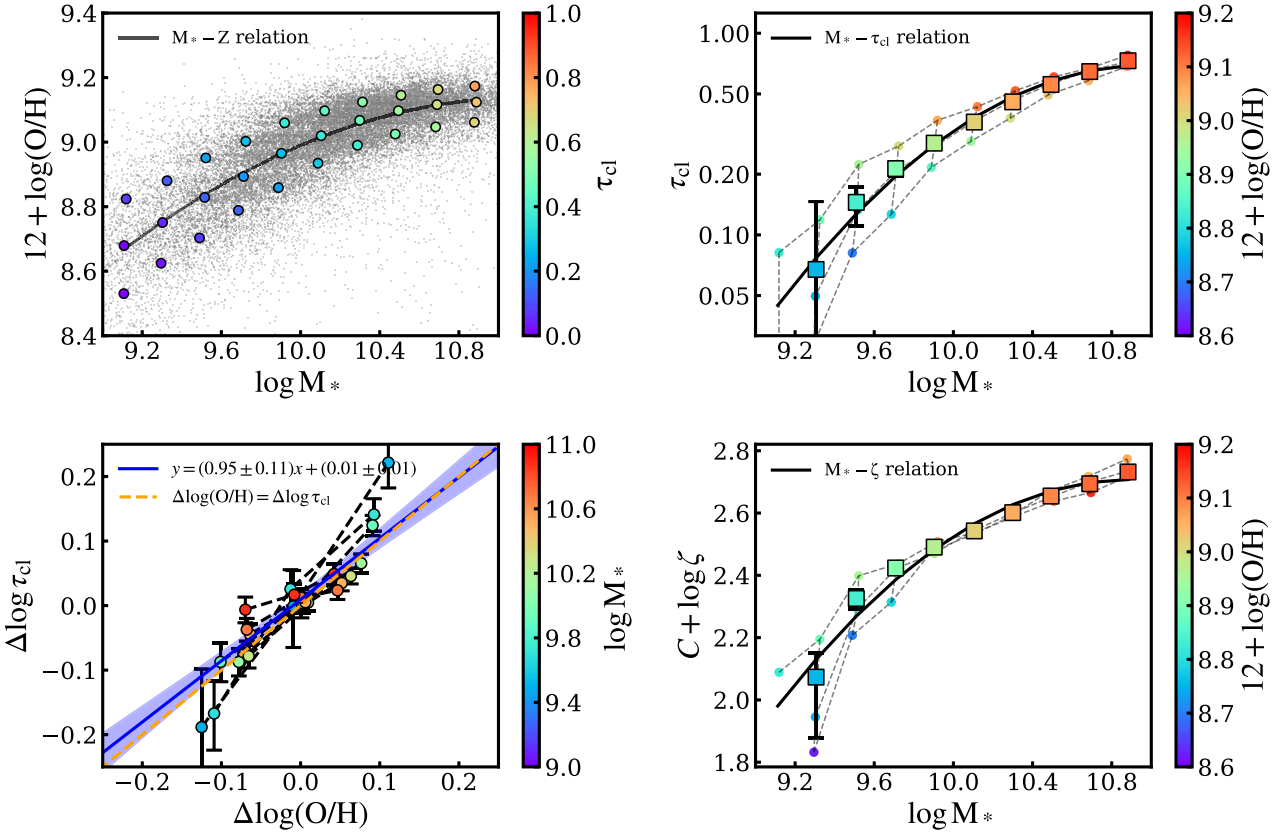

Figure 3. The dependence of $\tau_{\rm cl}$ on stellar mass M_* and metallicity 12+log(O/H). Top left panel: M_*–Z relation; $\tau_{\rm cl}$ is color-coded. The circles represent the 30 subsamples of galaxies in M_* and Z bins, while the small black dots in background are all sample galaxies. The solid curve is the fitted M_*–Z relation of Equation (6). Top right panel: M_*–$\tau_{\rm cl}$ relation; metallicity is color-coded. The dots connected by dotted lines represent the subsample of galaxies in 30 stellar mass and metallicity bins, while the squares show the median $\tau_{\rm cl}$ values in ten stellar mass bins irrespective of metallicity. The solid curve is the fitted M_*–$\tau_{\rm cl}$ relation of Equation (7). Bottom left panel: the residual $\Delta\log\tau_{\rm cl} - \Delta\log({\rm O/H})$ relation color-coded with the M_* of different stellar mass bins. The galaxy bins with the same stellar mass are connected by black dashed lines. The best fit and the confidence level of 1σ are shown by the blue solid curve and shadowed regions. The dashed orange diagonal line ($\Delta\log\tau_{\rm cl} = \Delta\log({\rm O/H})$) is plotted for comparison. Bottom right panel: M_*–ζ relation color-coded with the metallicity. The data points are the same as that of the top left panel. The solid curve follows Equation (9).

(12 + log(O/H)) of host galaxies using the simplified CCC model outlined in Section 3.

We first show the M_*–Z relation of all face-on SFGs with small dots in the the top left panel of Figure 3. We show the median 12 + log(O/H) as a function of stellar mass with the solid curve, which is parameterized by a quadratic function following Tremonti et al. (2004):[6]

$$12 + \overline{\log({\rm O/H})}(M_*) = -0.114(\log M_*)^2 + 2.534\log M_* - 4.978. \quad (6)$$

In addition, the subsamples of galaxies in 30 stellar mass and metallicity bins are shown by circle dots in this panel, whose color codes the τ_{cl} values of each subsample. As can be seen, more massive and more metal-rich galaxies have systematically higher $\tau_{\rm cl}$ values, ranging from $\tau_{\rm cl}\sim0.05$ for the least massive and metal-poor galaxies ($\log M_*\sim9$, 12 + log(O/H) ∼ 8.5) to $\tau_{\rm cl}\sim0.8$ for the most massive and metal-rich galaxies ($\log M_*\sim11$, 12 + log(O/H) ∼ 9.2).

To show the dependence of $\tau_{\rm cl}$ on stellar mass and metallicity clearly, we plot $\tau_{\rm cl}$ as a function of M_* in the top right panel of Figure 3, where the median 12 + log(O/H) of each sample galaxies is color-coded. We first show the median $\tau_{\rm cl}$ of sample galaxies in ten stellar mass bins, irrespective of their metallicity, as big squares. The $\tau_{\rm cl}$ of sample galaxies in 30 stellar mass and metallicity bins is then shown as circle dots connected by dotted lines. For clarity, we only show the uncertainties of $\tau_{\rm cl}$ for ten stellar mass bins. For the global median $\tau_{\rm cl}$ in 10 M_* bins (squares), we see that $\overline{\tau_{\rm cl}}$ increases monotonically with stellar mass. Following the M_*–Z relation, we also parameterize the $M_* - \overline{\tau_{\rm cl}}$ relation with a quadratic function and get the best fit

$$\log\overline{\tau_{\rm cl}}(M_*) = -0.343(\log M_*)^2 + 7.54\log M_* - 41.531, \quad (7)$$

which is shown as the black solid curve in this panel. Besides the M_*–Z degeneracy, again, we see a clear second-order dependence of $\tau_{\rm cl}$ on metallicity at given stellar mass: higher Z galaxies have higher $\tau_{\rm cl}$.

To show the second-order dependence of $\tau_{\rm cl}$ on Z more clearly, we plot the residual and the error of the M_*–$\tau_{\rm cl}$ relation ($\Delta\log\tau_{\rm cl}$) as function of the residual of the M_*–Z relation ($\Delta\log({\rm O/H})$) in the bottom left panel of Figure 3. Specifically, these two residuals are defined as

$$\Delta\log({\rm O/H}) = \log({\rm O/H}) - \overline{\log({\rm O/H})}(M_*),$$
$$\Delta\log\tau_{\rm cl} = \log\tau_{\rm cl} - \log\overline{\tau_{\rm cl}}(M_*), \quad (8)$$

[6] This fitting formula is obtained using curve_fit module in scipy library of Python3 and is very similar to that of Tremonti et al. (2004).

where $\overline{\log(\mathrm{O/H})}(M_*)$ and $\log\overline{\tau_{\rm cl}}(M_*)$ are defined by Equations (6) and (7), respectively. We also fit the global trend with a linear relation. The relation and its confidence level of 1σ are also plotted with the blue solid line and shadowed regions in the bottom left panel of Figure 3. As can be seen, after subtracting the $M_*-\overline{\tau_{\rm cl}}$ relation and $M_*-\overline{Z}$ relation, $\Delta\log\tau_{\rm cl}$ roughly shows a linear relation with $\Delta\log(\mathrm{O/H})$ for all M_* bins with a slope of 1. According to Equation (3), this equivalence implies that the DTM (ζ) of galaxies with different metallicity is roughly a constant at given stellar mass.

To further investigate the results shown above, we plot ζ (defined as Equation (3)) as a function of M_* only in the bottom right panel of Figure 3, color-coded according to the metallicity. Following the top right panel, we show the sample galaxies in ten stellar mass bins, irrespective of their metallicity, as big squares and these subsamples in 30 stellar mass and metallicity bins as circle dots connected by dotted lines. As can be seen, ζ almost shows no second-order dependence on metallicity for most stellar mass bins ($\log M_* > 9.8$). For these few low-mass bins, considering the uncertainties of ζ there, we believe ζ is also largely independent of metallicity. Even if there is a correlation, the correlation should be very weak. Since ζ is only a function of stellar mass, we provide an analytic expression of that function. Rather than fitting the data points in the bottom right panel, we can also obtain it by the combination of Equations (3), (6), (7), and (8),

$$\begin{aligned} C+\log\zeta &= \log\overline{\tau_{\rm cl}}(M_*)-\overline{\log(\mathrm{O/H})}(M_*)\\ &= -0.229(\log M_*)^2+5.006\log M_*-24.553. \end{aligned} \tag{9}$$

We plot this quadratic function as a solid curve in this panel. As can be seen, this derived analytic formula matches the data points very well.

From the plots shown above, we arrive at the main finding of this study: the DTM of a galaxy is a unique function of the stellar mass of its host galaxy. This finding has important implications for the timescale of dust-particle evolution, which will be further discussed in Section 5.2.

5. Discussion

Most of the studies on dust-evolution models focus on the dependence of ζ on metallicity (Lisenfeld & Ferrara 1998; Hirashita et al. 2002; Draine et al. 2007; Galametz et al. 2011; Zafar & Watson 2013; Rémy-Ruyer et al. 2014; Wiseman et al. 2017; Kahre et al. 2018; De Vis et al. 2019). The process of dust evolution consists of the dust production and destruction. The dust production is mainly motivated by dust formation in stellar winds and supernovae and grain growth in the ISM. The dust destruction is mainly related to star formation depletion, thermal sputtering, and supernova destruction. In addition, gas inflows and outflows also affect the amount of dust. Among these mechanisms, grain growth increases ζ, while dust destruction has the opposite effect. If there is no grain growth and dust destruction, ζ is a constant that depends on the yield of dust in stellar winds and supernovae. When there is a balance between dust grain growth and destruction, ζ is also a constant (i.e., Mattsson et al. 2012; De Vis et al. 2017). On the other hand, in dense and metal-rich environments (e.g., in the inner regions of molecular clouds), where the dust growth effect outweighs the destruction of dust particles, we would expect that ζ will increase with metallicity. In this Letter, we propose that the stellar mass of the host galaxy plays a more fundamental role in ζ of H II regions. In this section, we first discuss the ζ–Z relation implied by the M_*–ζ relation in our study (Section 5.1) and then explore possible physical mechanisms behind the M_*–ζ relation we propose (Section 5.2).

5.1. ζ–Z Relation

Many studies have discussed the dependence of ζ on Z (e.g., Silva et al. 1998; James et al. 2002; Somerville et al. 2012; Camps et al. 2015; Yajima et al. 2015; Clark et al. 2016; Katz et al. 2019; Ma et al. 2019). To have a good comparison of our study with earlier results, we also explore the dependence of ζ on Z only. Specifically, we divide our sample SFGs into ten metallicity bins in the range of $8.4 < 12+\log(\mathrm{O/H}) < 9.4$ with bin width of 0.1 dex and then calculate the median $\tau_{\rm cl}$ of the sample galaxies in each metallicity bin. Following Equation (3), we calculate ζ and then show its dependence on metallicity ($12+\log(\mathrm{O/H})$) in Figure 4, where the median $\log M_*$ of sample galaxies in each metallicity bin is color-coded. We see that ζ increases monotonically with $\log(\mathrm{O/H})$ at low-metallicity range ($12+\log(\mathrm{O/H}) < 9.0$). At the high-metallicity end ($12+\log(\mathrm{O/H}) > 9.0$), ζ is roughly a constant. Such a trend has been reported in early studies (e.g., Rémy-Ruyer et al. 2014).

For more quantitative comparisons, we also plot two suggested ζ–Z relations in the literature in Figure 4. One is the relation $\zeta\sim$ constant (Issa et al. 1990; Lisenfeld & Ferrara 1998) represented by the dashed line, where the intercept has been adjusted to fit the observed $\log\zeta$ at high metallicity. The other is the nonlinear relation $\zeta\propto Z^{1.45}$ (e.g., De Vis et al. 2019; Li et al. 2019). This relation is shown by the dotted–dashed line and the intercept also has been adjusted to fit the observed ζ–Z relation at low metallicity. As can be seen, these two known relations agree well with our results at low- and high-metallicity parts, respectively.

According to the dependence of $\tau_{\rm cl}$ on the two-dimensional M_* and Z bins shown in the top right panel of Figure 3, the slope of 1.45 between $\log\zeta$ and $\log(\mathrm{O/H})$ at the low-metallicity end shown in Figure 4 is more of the relation between $\tau_{\rm cl}$ and M_*, which also can be clearly viewed from the color (stellar mass) of data points. At the high-metallicity end, the M_*–Z relation becomes flat, and the M_*–$\tau_{\rm cl}$ relation for high mass (metallicity) galaxies also becomes flat. As a result, ζ is a constant. In summary, in our study, the observed ζ–Z relation is a joint result of the M_*–Z (Equation (6)) and M_*–ζ (Equation (9)) relation.

5.2. Physical Implications of the M_*–ζ Relation

The M_*–ζ relation we have derived has important physical implications on the assembly history of different components (e.g., stellar population, metal, dust) of galaxies.

The M_*–Z relation of local SFGs could be a result of higher surface density of more massive disk galaxies (Chang et al. 2010; Belfiore et al. 2017). Moreover, the star formation history of present-day galaxies shows a "downsizing" behavior, where the stars in more massive galaxies tend to be formed earlier and over a shorter time span (Neistein et al. 2006). Therefore, the higher Z of more massive galaxies could also be a result of the higher star formation efficiency at higher

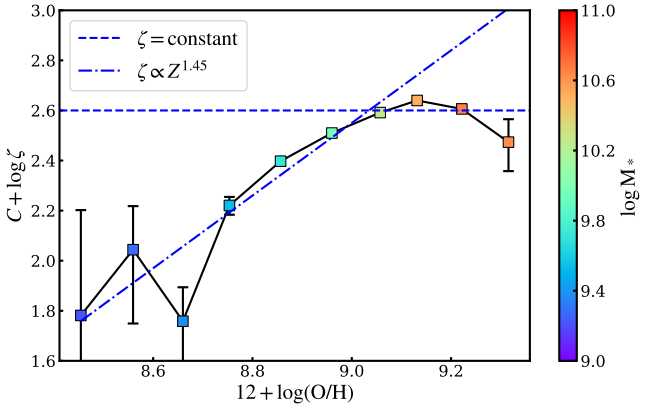

Figure 4. The dependence of $\log\zeta$ on 12+log(O/H) with stellar mass color-coded, where the $\log\zeta$ is interpreted by $\log\tau_{\rm cl} - \log({\rm O/H})$. The dotted–dashed line has a slope of 1.45, and the dashed line represents the DTM as a constant.

redshift, when the surface gas density of galaxies is higher on average (Fu et al. 2009). In general, the mass assembly history of galaxies is in the order of a few Gyr, which is much longer than the dust grain growth timescale in molecular clouds ($\sim10^7$–10^8 yr Galliano 2022). Therefore, considering that more massive galaxies assemble their metals earlier and the dust grain growth timescale is shorter in higher metallicity regions, it is natural that more massive galaxies have a higher ζ today.

On the other hand, the higher metallicity of more massive galaxies is possibly related to their deeper gravitational potential, where it is suggested that it is more difficult for outflows to escape from the host galaxy (Chang et al. 2010; Chisholm et al. 2017). Considering heavier mass of metal particles, for both the momentum and energy driven outflows, the metal particles naturally have lower outflow velocity and outflow rate than those of gas (Pandya et al. 2021). Predictably, the outflow fraction of dust grains would be even smaller than that of metal particles as the dust grains are much heavier than metal particles. Therefore, the outflow scenario also provides a reasonable explanation for the lower Z and ζ in less massive galaxies, where the outflow is more prominent.

At a given stellar mass, our study shows that ζ is independent of gas-phase metallicity. This phenomena is possibly related to the physical condition and lifetime of H II regions. For the outer layer of H II regions (or diffuse molecular cloud environments), the timescale of dust growth ($\sim$100 Myr; Galliano 2022) is much longer than the lifetime of H II regions ($\sim$10 Myr), and the temperature ($\sim10^4$K) is a large offset from the requirement of dust sputtering or sublimation ($\sim10^6$ K). In addition, the dust destruction effect by supernovae can also be neglected since living OB stars are needed for H II regions. Therefore, ζ does not have enough time to evolve during the short lifetime of H II regions. On the other hand, for galaxies at a given stellar mass, the linear correlation between metallicity and optical depth is probably related to the stochastic feeding (e.g., metal-poor gas accretion) of SFG, which is a transient process and has been used to explain the local anticorrelation between star formation rate and gas-phase metallicity (Sánchez Almeida & Sánchez-Menguiano 2019). In this scenario, the stochastic feeding of metal-poor gas in short timescales does not change either the total amount of metal or dust; that is, this kind of inflow causes a simultaneous decrease of both metallicity and DTG (τ_{cl}) and therefore does not affect ζ.

6. Summary

In this study, by applying a simplified version of the CCC model of Lu et al. (2022) on a sample of face-on SFGs selected from SDSS, we obtain the typical dust optical depth τ_{cl} of the H II regions for galaxies in different stellar mass and gas-phase metallicity bins. By investigating the dependence of τ_{cl} on M_* and Z and linking τ_{cl} to the DTG of galaxies, we generate the following conclusions on the DTG and DTM of SFGs.

We find that $\tau_{\rm cl}$ increases with M_* faster than Z so that the DTM ($\zeta\sim\tau_{\rm cl}/Z$) increases with M_* of galaxies. At a given stellar mass, the residual $\Delta\log\tau_{\rm cl}$ is linearly correlated with $\Delta\log({\rm O/H})$, implying a constant ζ. Our results show that the stellar mass of galaxies is the first parameter in the DTM–Z relation of galaxies, like in many other scaling relations (e.g., Kauffmann et al. 2003b; Shen et al. 2003; Peng et al. 2010). The ζ–Z relation discussed in literature is a joint result of the M_*–ζ and M_*–Z relation.

We thank the anonymous referee for the helpful and constructive comments that improved the paper. This work is supported by the National Natural Science Foundation of China (No. 12073059 & No. U2031139), the National Key R&D Program of China (No. 2019YFA0405501), an the Program of Shanghai Academic/Technology Research Leader (22XD1404200). We also acknowledge the science research grants from the China Manned Space Project with NO. CMS-CSST-2021-A04, CMS-CSST-2021-A07, CMS-CSST-2021-A08, CMS-CSST-2021-A09, CMS-CSST-2021-B04. F.T.Y. acknowledges support by the Funds for Key Programs of Shanghai Astronomical Observatory (No. E195121009) and the Natural Science Foundation of Shanghai (Project Number: 21ZR1474300).

Funding for the SDSS and SDSS-II has been provided by the Alfred P. Sloan Foundation, the Participating Institutions, the National Science Foundation, the U.S. Department of Energy, the National Aeronautics and Space Administration, the Japanese Monbukagakusho, the Max Planck Society, and the Higher Education Funding Council for England. The SDSS Web Site is http://www.sdss.org/.

The SDSS is managed by the Astrophysical Research Consortium for the Participating Institutions. The Participating Institutions are the American Museum of Natural History, Astrophysical Institute Potsdam, University of Basel, University of Cambridge, Case Western Reserve University, University of Chicago, Drexel University, Fermilab, the Institute for Advanced Study, the Japan Participation Group, Johns Hopkins University, the Joint Institute for Nuclear Astrophysics, the Kavli Institute for Particle Astrophysics and Cosmology, the Korean Scientist Group, the Chinese Academy of Sciences (LAMOST), Los Alamos National Laboratory, the Max-Planck-Institute for Astronomy (MPIA), the Max-Planck-Institute for Astrophysics (MPA), New Mexico State University, Ohio State University, University of Pittsburgh, University of Portsmouth, Princeton University, the United States Naval Observatory, and the University of Washington.

ORCID iDs

Jiafeng Lu
(卢家风) https://orcid.org/0000-0002-8817-4587
Shiyin Shen
(沈世银) https://orcid.org/0000-0002-3073-5871

Fang-Ting Yuan
(袁方婷) https://orcid.org/0000-0001-6763-5869
Qi Zeng (曾琪) https://orcid.org/0000-0002-4638-2580

References

Belfiore, F., Maiolino, R., Tremonti, C., et al. 2017, MNRAS, 469, 151
Bruzual, G., & Charlot, S. 2003, MNRAS, 344, 1000
Calzetti, D., Armus, L., Bohlin, R. C., et al. 2000, ApJ, 533, 682
Camps, P., Misselt, K., Bianchi, S., et al. 2015, A&A, 580, A87
Chang, R. X., Hou, J. L., Shen, S. Y., & Shu, C. G. 2010, ApJ, 722, 380
Chisholm, J., Tremonti, C. A., Leitherer, C., & Chen, Y. 2017, MNRAS, 469, 4831
Cid Fernandes, R., Mateus, A., Sodré, L., Stasińska, G., & Gomes, J. M. 2005, MNRAS, 358, 363
Clark, C. J. R., Schofield, S. P., Gomez, H. L., & Davies, J. I. 2016, MNRAS, 459, 1646
De Vis, P., Gomez, H. L., Schofield, S. P., et al. 2017, MNRAS, 471, 1743
De Vis, P., Jones, A., Viaene, S., et al. 2019, A&A, 623, A5
Draine, B. T., Dale, D. A., Bendo, G., et al. 2007, ApJ, 663, 866
Draine, B. T., & Salpeter, E. E. 1979, ApJ, 231, 438
Edmunds, M. G. 2001, MNRAS, 328, 223
Fitzpatrick, E. L., Massa, D., Gordon, K. D., Bohlin, R., & Clayton, G. C. 2019, ApJ, 886, 108
Fu, J., Hou, J. L., Yin, J., & Chang, R. X. 2009, ApJ, 696, 668
Galametz, M., Madden, S. C., Galliano, F., et al. 2011, A&A, 532, A56
Galliano, F. 2022, Habilitation Thesis, Univ. Paris-Saclay
Hirashita, H. 1999, ApJ, 522, 220
Hirashita, H., Tajiri, Y. Y., & Kamaya, H. 2002, A&A, 388, 439
Issa, M. R., MacLaren, I., & Wolfendale, A. W. 1990, A&A, 236, 237
James, A., Dunne, L., Eales, S., & Edmunds, M. G. 2002, MNRAS, 335, 753
Kahre, L., Walterbos, R. A., Kim, H., et al. 2018, ApJ, 855, 133
Katz, H., Laporte, N., Ellis, R. S., Devriendt, J., & Slyz, A. 2019, MNRAS, 484, 4054
Kauffmann, G., Heckman, T. M., Tremonti, C., et al. 2003a, MNRAS, 346, 1055
Kauffmann, G., Heckman, T. M., White, S. D. M., et al. 2003b, MNRAS, 341, 33
Li, L., Shen, S., Hou, J., et al. 2017, AJ, 153, 88
Li, Q., Narayanan, D., & Davé, R. 2019, MNRAS, 490, 1425
Lisenfeld, U., & Ferrara, A. 1998, ApJ, 496, 145
Liu, G., Calzetti, D., Kennicutt, R. C. J., et al. 2013, ApJ, 772, 27
Lu, J., Shen, S., Yuan, F.-T., et al. 2022, ApJ, 938, 139
Ma, X., Hayward, C. C., Casey, C. M., et al. 2019, MNRAS, 487, 1844
Mattsson, L., Andersen, A. C., & Munkhammar, J. D. 2012, MNRAS, 423, 26
Mattsson, L., Gomez, H. L., Andersen, A. C., et al. 2014, MNRAS, 444, 797
Neistein, E., van den Bosch, F. C., & Dekel, A. 2006, MNRAS, 372, 933
Oey, M. S., Parker, J. S., Mikles, V. J., & Zhang, X. 2003, AJ, 126, 2317
Pandya, V., Fielding, D. B., Anglés-Alcázar, D., et al. 2021, MNRAS, 508, 2979
Peng, Y.-j., Lilly, S. J., Kovač, K., et al. 2010, ApJ, 721, 193
Rémy-Ruyer, A., Madden, S. C., Galliano, F., et al. 2014, A&A, 563, A31
Sánchez Almeida, J., & Sánchez-Menguiano, L. 2019, ApJL, 878, L6
Santoro, F., Kreckel, K., Belfiore, F., et al. 2022, A&A, 658, A188
Shen, S., Mo, H. J., White, S. D. M., et al. 2003, MNRAS, 343, 978
Silva, L., Granato, G. L., Bressan, A., & Danese, L. 1998, ApJ, 509, 103
Somerville, R. S., Gilmore, R. C., Primack, J. R., & Domínguez, A. 2012, MNRAS, 423, 1992
Tremonti, C. A., Heckman, T. M., Kauffmann, G., et al. 2004, ApJ, 613, 898
Wiseman, P., Schady, P., Bolmer, J., et al. 2017, A&A, 599, A24
Yajima, H., Shlosman, I., Romano-Díaz, E., & Nagamine, K. 2015, MNRAS, 451, 418
Zafar, T., & Watson, D. 2013, A&A, 560, A26